Automatic Navigation of Microswarms for Dynamic Obstacle Avoidance

Yuezhen Liu, *Student Member, IEEE*, Hui Chen*, Student Member, IEEE*, Qian Zou, *Student Member, IEEE*,
Xingzhou Du, *Member, IEEE*, Yibin Wang, *Student Member, IEEE*, and Jiangfan Yu, *Member, IEEE*

***Abstract*—Control and navigation of microrobotic swarms have drawn extensive attention recently. Avoiding dynamic obstacles using swarms is one of the major challenges that still remain unsolved. In this work, we develop a control strategy to navigate microrobotic swarms to targeted positions while avoiding dynamic obstacles. We first propose a criterion to evaluate the real-time locomotion efficiency during dynamic obstacle avoidance, i.e., the swarm moving direction and the distance between the swarm and the target. Subsequently, a hierarchical radar with three functional boundaries (detection, safety, and prediction circle) is designed for swarms. The optimal moving direction of the swarm with the existence of dynamic obstacles is selected based on the three circles. The effectiveness of the algorithm is validated by simulations and experiments. Using the proposed strategy, the swarm is capable of avoiding multiple moving obstacles and reaching the predefined target. Finally, to show the compatibility of the proposed control method, the swarm is deployed in a micromaze with different dynamic obstacles, and the results also validate the effectiveness of the strategy.**

***Index Terms*—Automation at micro-nanoscale, microrobotics, swarm control.**

I. INTRODUCTION

RECENTLY, untethered magnetic microrobots have attracted extensive attention due to their immense potential in target drug delivery, biosensing, and micromanipulation [1], [2], [3], [4], [5], [6], [7], [8], [9]. Various kinds of microrobots have been investigated, such as helical-shaped microswimmers [10], [11], [12], [13], [14], soft millirobots [15], [16], [17], [18], [19], [20], and bacteria [21], [22], [23], [24]. However, single microrobots may have a critical limitation when performing cargo/drug delivery due to their small sizes and volumes. In addition, it is challenging to realize the real-time *in vivo* imaging of a single microrobot [25]. By contrast, microswarms composed of a large number of nanoagents can serve as promising candidates [26], [27], [28].

Control and navigation of microswarms have been investigated over the past few years. Different from macroscale robots that can be equipped with varied sensors and controllers [29], microswarms without on-board sensors and controllers are hard to be precisely manipulated. A statistics-based strategy is developed to automatically generate, identify, and control vortex-like swarms, and the swarms are able to track the desired trajectory with small distance errors [30]. An adaptive control method is proposed to simultaneously control the aspect ratio, long-axis orientation, and position of elliptical swarms [31]. To track the microswarm in real time, an ultrasound Doppler imaging–guided approach is proposed, and the localized delivery of the microswarm in vascular system can be achieved using the method [32]. Different control schemes have been adopted to navigate microswarms in complex or confined environments, but the navigation of microswarms in the environment with dynamic obstacles is still a challenge that remains unsolved.

To avoid obstacles at the microscale, several strategies have been developed. The image-based visual servoing and path planning method are used to control a helical swimmer [33], spore-based magnetic microrobots [34], and two microrobots [35] to follow desired paths while avoiding static obstacles. A microvehicle can avoid a single dynamically moving obstacle using global path planning and fuzzy logic approach [36], but the navigation of the microrobot in a more complicated scenario with multiple dynamic obstacles is challenging. Global path planning adopted by the aforementioned methods taking all the obstacles and boundaries into consideration leads to a heavy computation load, which hinders real-time control of the microrobots [37]. Several techniques have been proposed for the avoidance of a dynamic obstacle at the macroscale [38], such as potential field method [39], genetic algorithm-based path planning [40], and data-driven fuzzy approach [41]. However, these methods regard the robot as a nondeformable object, and

---

Manuscript received 29 September 2022; revised 14 February 2023; accepted 28 March 2023. Date of publication 19 April 2023; date of current version 8 August 2023. This work was supported in part by National Natural Science Foundation of China Project 62103347, in part by the Shenzhen Science and Technology Program under Grant RCBS20210609103155061, in part by the start-up funding of CUHK-Shenzhen under Grant UDF01001929, and in part by the Shenzhen Institute of Artificial Intelligence and Robotics for Society. This paper was recommended for publication by Associate Editor M. Kim and Editor A. Menciassi upon evaluation of the reviewers' comments. *(Yuezhen Liu and Hui Chen contributed equally to this work.) (Corresponding author: Jiangfan Yu.)*

Yuezhen Liu, Hui Chen, Qian Zou, Xingzhou Du, and Yibin Wang are with the School of Science and Engineering, The Chinese University of Hong Kong, Shenzhen 518172, China, and also with the Shenzhen Institute of Artificial Intelligence and Robotics for Society (AIRS), Shenzhen 518129, China (e-mail: yuezhenliu@link.cuhk.edu.cn; huichen1@link.cuhk.edu.cn; qianzou@link.cuhk.edu.cn; duxingzhou@cuhk.edu.cn; yibinwang@link.cuhk.edu.cn).

Jiangfan Yu is with the School of Science and Engineering, The Chinese University of Hong Kong, Shenzhen 518172, China, also with the Shenzhen Institute of Artificial Intelligence and Robotics for Society (AIRS), Shenzhen 518129, China, and also with the School of Medicine and the School of Life and Health Science, The Chinese University of Hong Kong, Shenzhen 518172, China (e-mail: yujiangfan@cuhk.edu.cn).

This article has supplementary material provided by the authors and color versions of one or more figures available at https://doi.org/10.1109/TRO.2023.3263773.

Digital Object Identifier 10.1109/TRO.2023.3263773

the techniques that control deformable robotic swarms at the microscale to perform dynamic obstacle avoidance still require further investigations.

Inspired by the technique of radar detection, this article proposes a radar-based control strategy to navigate a microrobotic swarm to targeted positions while avoiding dynamic obstacles. In this article, we first introduce the kinematic model of vortex-like swarms and the evaluation criterion of the real-time locomotion efficiency during dynamic obstacle avoidance. The hierarchical radar with three functional boundaries (detection, safety, and prediction circle) is then developed for the swarms, and the size of the hierarchical radar can adjust automatically according to the changing size of the vortex-like swarm. The control strategy based on the hierarchical radar and the visual feedback is proposed. To validate the functions of the three circles, the simulation and experimental results of avoiding a single dynamic obstacle utilizing the hierarchical radar with different configurations are conducted. The swarm is also capable of reaching the target while avoiding multiple moving obstacles, which indicates the effectiveness of the proposed strategy in a complicated scenario. The navigation of the swarm in a micromaze with different types of dynamic obstacles is also demonstrated, revealing the high compatibility of the radar-based algorithm.

The main contributions of this article include the following. 1) A criterion to evaluate the efficiency of dynamic obstacle avoidance is proposed. The criterion is capable of showing the real-time locomotion efficiency during dynamic obstacle avoidance. 2) A radar-based algorithm for dynamic obstacle avoidance is developed. Optimal moving direction of the swarm during avoidance can be decided by the radar-based algorithm. 3) The control strategy combining visual feedback and the radar-based algorithm is proposed. Using the strategy, the swarm can be navigated to the target when avoiding multiple moving obstacles and varied obstacles in a micromaze. The effectiveness of the strategy is validated by experiments.

II. MODELS AND DEFINITIONS

A. Kinematic Model of Vortex-Like Swarm

A vortex-like swarm can be formed and actuated using rotating magnetic fields [42]. Rotating fields can be expressed as

$$B = [B_x B_y B_z]^T = A\begin{bmatrix} -\cos(\varphi)\cos(\theta)\cos(2\pi ft) - \sin(\theta)\sin(2\pi ft) \\ -\cos(\varphi)\sin(\theta)\cos(2\pi ft) + \cos(\theta)\sin(2\pi ft) \\ \sin(\varphi)\cos(2\pi ft) \end{bmatrix} \quad (1)$$

where A and f are the amplitude and the frequency of the magnetic field, respectively.

By adding a pitch angle φ, the swarm will move along the direction angle θ. If the pitch angle is applied within the limitation before the swarm loses its stability, a stable morphology of the swarm will be maintained. In addition, the applied pitch angle and the swarm velocity have a linear relationship [30]. The position of the swarm is denoted by $P = [P_x(t), P_y(t)]^T$, and when the minor external disturbance is neglected, the kinematic model of the swarm can be expressed as

$$\begin{cases} \dot{P}_x(t) = c\varphi(t)\cos(\theta(t)) \\ \dot{P}_y(t) = c\varphi(t)\sin(\theta(t)) \end{cases} \quad (2)$$

where c is a positive constant obtained by experimental calibration [30].

B. Real-Time Efficiency Criterion of Dynamic Obstacle Avoidance

Conventionally, the overall locomotion efficiency is indicated by the total length of locomotion path [43], [44], i.e., a short path from the starting point to the target indicates a high overall locomotion efficiency. However, in addition to the overall locomotion efficiency, the real-time locomotion efficiency, i.e., the tendency of taking the shortest path to the target, also needs to be evaluated. The reason is that the real-time locomotion efficiency changes rapidly based on the moving of the dynamic obstacles, and the overall locomotion efficiency cannot represent the real-time locomotion efficiency. In addition, based on the real-time locomotion efficiency during dynamic obstacle avoidance, the performance of dynamic obstacle avoidance at different time can be obtained, and the control strategy can be optimized correspondingly. Herein, we propose a criterion to evaluate the real-time locomotion efficiency during dynamic obstacle avoidance, which is denoted as avoidance efficiency.

To explain the criterion, the schematics of dynamic obstacle avoidance is shown in Fig. 1(a). The swarm is moving from the starting point (i.e., the blue dot) to the target (i.e., the green dot). When the dynamic obstacle has a large distance between the swarm, the moving direction of the swarm is not influenced by the obstacle O_{ob}. Therefore, the swarm will move along the shortest linking between the swarm and the target $\overrightarrow{O_sO_t}$, and the velocity is denoted by $\boldsymbol{v}_t$ (i.e., the black arrow). When the distance between the swarm and the obstacle is short, the velocity of the swarm changes to $\boldsymbol{v}_s$ (i.e., the orange arrow) in order to avoid the collision. In this case, the direction deviation between the swarm moving direction $\overrightarrow{v_s}$ and $\overrightarrow{v_t}$ is α, which can be expressed as

$$\alpha = \cos^{-1}\left(\frac{\boldsymbol{v}_s \cdot \boldsymbol{v}_t}{\|\boldsymbol{v}_s\|\,\|\boldsymbol{v}_t\|}\right). \quad (3)$$

A large α reflects that the swarm has a tendency of passing a longer path to finally reach the target, which will decrease the avoidance efficiency. Meanwhile, if the distance between the swarm and the target l is large when the swarm is performing avoidance from obstacles, the total path that the swarm tends to have will also be longer. Hence, α and l determine the avoidance efficiency. The avoidance efficiency is indicated by the avoidance cost δ, i.e., a large avoidance cost δ reflects a tendency of having a longer path, and also a low avoidance efficiency. The avoidance cost δ can be expressed as

$$\delta = \begin{cases} \frac{l(1-\cos\alpha)}{l_0} & \text{obstacles exist} \\ 0 & \text{no obstacles} \end{cases} \quad (4)$$

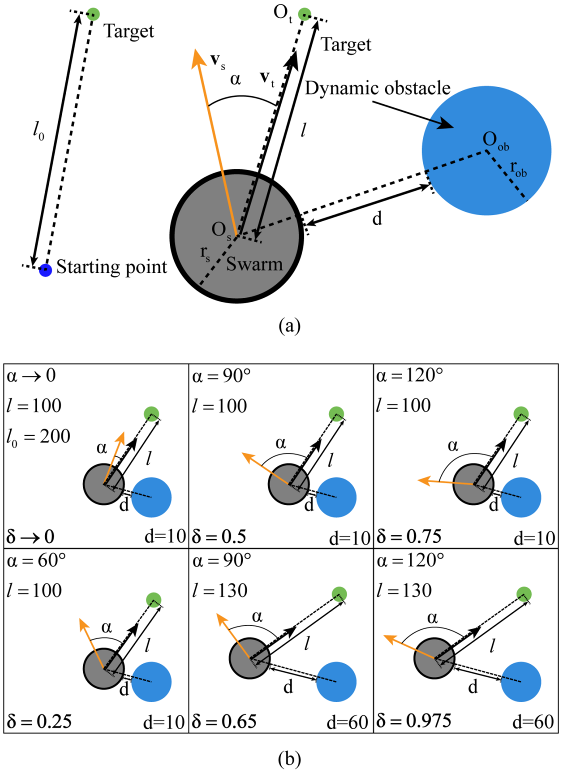

(a)

(b)

Fig. 1. Schematics of dynamic obstacle avoidance and the avoidance cost δ with different direction deviation α, swarm center-target center distance l, and the distance between the swarm and the obstacle d. (a) The schematics of dynamic obstacle avoidance. (b) The avoidance cost δ with different direction deviation α, swarm center-target center distance l, and the distance between the swarm and the obstacle d. The blue and grey circles represent the dynamic obstacle and the swarm, respectively. The blue and green dots indicate the starting point and the target, respectively. The centers of the swarm, the obstacle, and the target are O_s, O_{ob}, and O_t, respectively. The radii of the swarm and the obstacle are r_s and r_{ob}, respectively. The orange and black arrows indicate the swarm moving direction during avoidance and the moving direction when the swarm is not influenced by the obstacle.

where l_0 is the distance between the starting point and the target, as shown in Fig. 1(a), and α and l can be obtained at each time moment. In (4), the function of α is to indicate the influence of the dynamic obstacle on the moving direction of the swarm. The function of l is to give a weight for the direction deviation α, since the influence of the same α on the total length of the locomotion path is different when l changes. It is noted that, if the obstacle is not circular, the avoidance cost can still be calculated using (4).

The avoidance cost δ with different conditions are shown in Fig. 1(b). The distance between the starting point and the target l_0 is 200 pixels. The avoidance cost δ changes with the direction deviation α, and its lowest value approaches zero based on (4). When the direction deviation α is 60° and the distance between the centers of the swarm and the target l is 100 pixels, the avoidance cost δ is 0.25, which denotes a high avoidance efficiency. When l increases to 130 pixels and α is 90°, the avoidance cost δ becomes larger (i.e., $\delta = 0.65$). In this case, the avoidance efficiency is low, and the total path thus tends to be long. Based on Fig. 1(b), during the avoidance process, the increase of the distance between the swarm and the obstacle d (i.e., from 10 pixels to 60 pixels) leads to a larger l (i.e., from 100 pixels to 130 pixels), which increases the avoidance cost δ. As shown in Fig. 1(b), based on the criterion we proposed, with the increasing of α and l, δ increases significantly, indicating that the avoidance efficiency decreases. Therefore, the proposed criterion can well describe the avoidance efficiency.

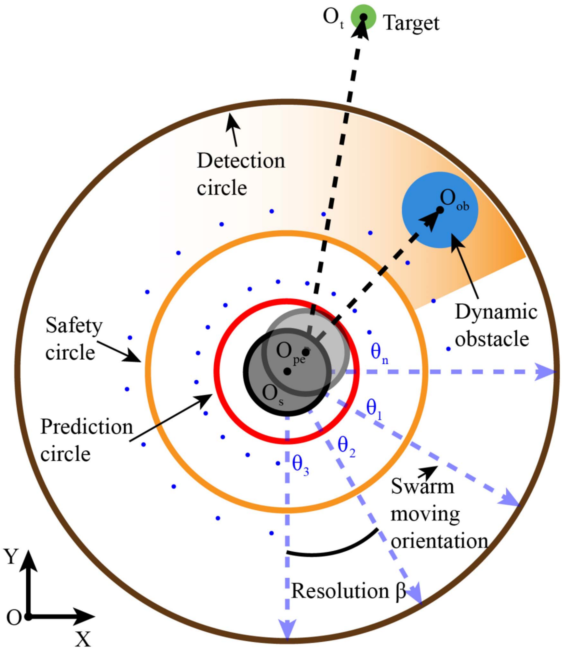

Fig. 2. Schematic diagram of the hierarchical radar. The brown, orange, and red circles indicate the detection, safety, and prediction circle, respectively. The grey, transparent grey, and blue circles indicate the swarm, the predictive swarm, and the dynamic obstacle, respectively. The green dot is the target. The centers of the swarm, the predictive swarm, the obstacle, and the target are O_s, O_{pe}, O_{ob}, and O_t, respectively. The blue dashed arrows represent alternative swarm moving directions $\theta_1, \theta_2 \ldots \theta_n$.

III. RADAR-BASED CONTROL STRATEGY

In order to increase the avoidance efficiency, we aim to decrease the value of δ and guarantee that no collision between the swarm and the obstacle occurs. Therefore, we develop a radar-based control strategy to detect the obstacle and find the optimal moving direction of the swarm during avoidance.

A. *Configuration of Hierarchical Radar*

Hierarchical radar is the key component in radar-based control algorithm, whose schematics is shown in Fig. 2. The radar consists of three functional boundaries, i.e., a prediction circle, a safety circle, and a detection circle. The radar generates alternative moving directions of the swarm by dividing all directions around the swarm into multiple units uniformly, and the angle resolution is β, as shown in Fig. 2. The number of the alternative moving directions of the swarm is $360/\beta$, and the ith moving direction is denoted by θ_i.

Herein, we define a predictive swarm, i.e., the one that is the current swarm moving along one of the alternative directions after a short moment, as shown by the transparent grey circle in Fig. 2. Each predictive swarm corresponds to an alternative moving direction. The position of the ith predictive swarm is denoted by $P_e(t,i) = [P_{ex}(t,i), P_{ey}(t,i)]^T$, and the ith alternative moving direction can then be expressed as

$$\theta_i(t) = \arctan\left(\frac{P_{ey}(t,i) - P_y(t)}{P_{ex}(t,i) - P_x(t)}\right) \tag{5}$$

where $P(t) = [P_x(t), P_y(t)]^T$ is the position of the current swarm.

The prediction circle is the circumcircle of all predictive swarms, as shown by the red circle in Fig. 2. The radius of the prediction circle can be expressed as

$$r_p = r_s + d_p \tag{6}$$

where r_s is the radius of the swarm, and d_p is the distance between the current swarm center and the predictive swarm center.

Based on (6), by setting a negligibly small d_p (i.e., not larger than 0.125 body lengths of the swarm), the radius of the prediction circle r_p is small (i.e., not larger than 0.625 body lengths of the swarm). In this case, the positions of the predictive swarm and the current swarm can be regarded as the same, and the direction obtained by the predictive swarm based on (5) can be applied as the moving direction of the current swarm. Meanwhile, a high collision risk exists when the obstacle enters the prediction circle. In addition, d_p has a lower limitation, e.g., 0.05 body lengths of the swarm, otherwise the swarm will not have sufficient time to avoid the obstacle if the obstacle enters the prediction circle.

The detection circle (i.e., the brown circle) serves as a trigger for obstacle avoidance, i.e., when the obstacle enters the detection circle, the avoidance strategy will be activated. The safety circle (i.e., the orange circle) is applied to exclude the unsafe alternative moving directions. The radii of the detection circle and the safety circle are shown in Fig. 3, which can be expressed as

$$\begin{cases} r_d = r_s + d_r \\ r_f = r_s + d_p + d_f \end{cases} \tag{7}$$

where r_d and r_f are the radii of the detection circle and the safety circle, respectively. The detection range and the safe distance are represented using d_r and d_f, respectively. Detailed functions of the prediction circle, the safety circle, and the detection circle will be elaborated in Section III-B.

B. Selection of the Optimal Moving Direction of the Swarm

From Section III-A, there are $360/\beta$ alternative moving directions in the hierarchical radar, and they form a set χ_0, which can be expressed as

$$\chi_0 = \left\{\theta \,\middle|\, \theta_i = \arctan\left(\frac{P_{ey}(t,i) - P_y(t)}{P_{ex}(t,i) - P_x(t)}\right) \right.$$
$$\left. i = 1, 2, \ldots, 360/\beta \right\}. \tag{8}$$

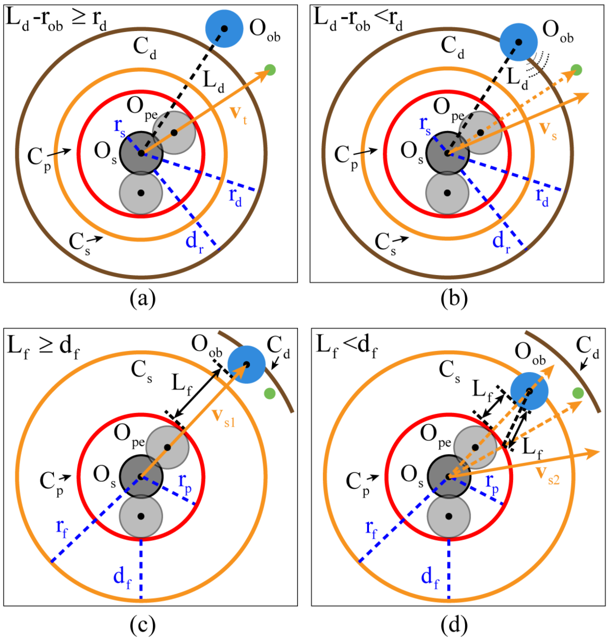

Fig. 3. Schematic description of the functions of the detection circle and the safety circle. (a)–(b) The schematic description of the function of the detection circle. (c)–(d) The schematic description of the function of the safety circle. The grey, transparent grey, and blue circles are the swarm, the predictive swarm, and the dynamic obstacle, respectively. The green dot is the target. The centers of the swarm, the predictive swarm, and the obstacle are O_s, O_{pe}, and O_{ob}, respectively. The distance between O_s and O_{ob} is L_d. The brown, orange, and red circles are the detection (C_d), safety (C_s), and prediction circle (C_p), respectively. The radii of the detection, safety, and prediction circle are r_d, r_f, and r_p, respectively. The detection range and the safe distance are d_r and d_f, respectively. The orange and dashed orange arrows represent the valid and invalid moving direction of the swarm, respectively.

Based on the positions of the predictive swarm, the dynamic obstacle, and the target, a selection function for obtaining the optimal moving direction can be expressed as

$$\phi_i = q_t N\left(\frac{1}{\left\|\overrightarrow{{}^iO_{pe}O_t}\right\|}\right) + q_a N\left(\left\|\overrightarrow{{}^iO_{pe}O_{ob}}\right\| - r_s - r_{ob}\right) \tag{9}$$

where ${}^iO_{pe}$, O_t, and O_{ob} are the centers of the ith predictive swarm corresponding to the ith alternative direction θ_i, the target and the dynamic obstacle, respectively. The Euclidean norm of the vector from the ith predictive swarm center to the target center is $\|\overrightarrow{{}^iO_{pe}O_t}\|$, and $\|\overrightarrow{{}^iO_{pe}O_{ob}}\|$ is the Euclidean norm of the vector from the ith predictive swarm center to the dynamic obstacle center. $N(\cdot)$ is the normalization in order to keep the terms $\frac{1}{\|\overrightarrow{{}^iO_{pe}O_t}\|}$ and $\|\overrightarrow{{}^iO_{pe}O_{ob}}\| - r_s - r_{ob}$ in a same range, i.e., from 0 to 1. It is noted that, if the obstacle is not circular, $\|\overrightarrow{{}^iO_{pe}O_{ob}}\| - r_s - r_{ob}$ in (9) will be converted to the distance between the edge of the predictive swarm and that of the obstacle.

In (9), a larger $\frac{1}{\|\overrightarrow{{}^iO_{pe}O_t}\|}$ indicates that the selected direction has a higher tendency of approaching the target, and a larger $\|\overrightarrow{{}^iO_{pe}O_{ob}}\| - r_s - r_{ob}$ indicates the selected direction has a higher tendency of avoiding the obstacle. The target weight and the avoidance weight are q_t and q_a, respectively. By tuning q_t and q_a, the proportion of the two tendencies will change when selecting the direction, based on (9). In order to automatically tune the proportion, q_t and q_a are obtained by the following equation:

$$\begin{bmatrix} q_t \\ q_a \end{bmatrix} = \begin{bmatrix} 1 \\ 0.5 \end{bmatrix} + \begin{bmatrix} \frac{k_t}{\frac{1}{2}{r_d}^2} & 0 \\ 0 & \frac{k_a}{\left(\frac{1}{r_s+r_{ob}} - \frac{1}{r_d}\right)^2} \end{bmatrix} \begin{bmatrix} Q_t \\ Q_a \end{bmatrix} \tag{10}$$

where k_t and k_a are positive constants that keep q_t larger than q_a.

In (10), Q_t and Q_a are set inspired by the artificial potential field method [45], which can be expressed as

$$Q_t = \frac{1}{2}\varepsilon \left\| \overrightarrow{O_s O_t} \right\|^2 \tag{11}$$

$$Q_a = \frac{1}{2}\eta \left(\frac{1}{\left\| \overrightarrow{O_s O_{ob}} \right\|} - \frac{1}{r_d} \right)^2 \tag{12}$$

where ε and η are the gravitational scale factor and the repulsive field factor, respectively.

From (10), q_t is kept larger than q_a. In this case, when selecting the direction, the priority of the swarm approaching the target is higher than that of avoiding obstacles, in order to make sure that the swarm can reach the target finally instead of keeping avoiding obstacles. In addition, if the radius of the detection circle r_d is larger, or the obstacle is closer to the swarm, the influence of the obstacle is considered larger, and thus, q_a increases.

In (9), the direction quality of the ith direction is ϕ_i, which is the sum of the two different tendencies under the corresponding weight q_t and q_a. The direction with the largest ϕ_i is the optimal direction that keeps the balance between approaching the target and avoiding the obstacle. The position of the predictive swarm corresponding to the direction with largest ϕ_i can be reversely deduced as $P_e(t, \text{opt}) = \arg\max(\phi_i)$.

Based on (5), the optimal moving direction of the swarm can then be expressed as

$$\theta_{\text{opt}}(t) = \arctan\left(\frac{P_{ey}(t, \text{opt}) - P_y(t)}{P_{ex}(t, \text{opt}) - P_x(t)} \right). \tag{13}$$

The optimal moving direction is obtained based on the set χ_0 in (8). However, the set χ_0 needs to be further screened based on the functions of the detection circle and the safety circle, in order to become the final set for the optimal direction selection.

The function of the detection circle is shown in Fig. 3(a) and (b). If the dynamic obstacle is out of the detection circle (i.e., $L_d - r_{ob} \geq r_d$), as shown in Fig. 3(a), the obstacle will be neglected, and the term $q_a N(\|\overrightarrow{{}^iO_{pe} O_{ob}}\| - r_s - r_{ob})$ in (9), which is about the dynamic obstacle avoidance, will be eliminated. As a result, only the term $q_t N(\frac{1}{\|\overrightarrow{{}^iO_{pe} O_t}\|})$ exists, which is about approaching the target. The selected direction thus has the highest tendency to approach the target. If the resolution β is sufficiently small (i.e., less than 1°), the selected direction is pointing approximately from the current swarm toward the target, which is the direction of $\boldsymbol{v}_t$ in Fig. 3(a). The selected moving direction in this case is

$$\theta_f = \arctan\left(\frac{P_{ty} - P_y(t)}{P_{tx} - P_x(t)} \right) \tag{14}$$

where $[P_{tx}, P_{ty}]^T$ is the position of the target. The set of alternative directions when the obstacle is out of the detection circle can then be expressed as

$$\chi_F = \{\theta \,|\theta = \theta_f \}. \tag{15}$$

However, as shown in Fig. 3(b), when the dynamic obstacle enters the detection circle (i.e., $L_d - r_{ob} < r_d$), the obstacle is taken into consideration when selecting the optimal direction, and thus, the term $q_a N(\|\overrightarrow{{}^iO_{pe} O_{ob}}\| - r_s - r_{ob})$ in (9) remains for consideration. With the influence of the dynamic obstacle, the optimal moving direction of the swarm changes from $\overrightarrow{v_t}$ to $\overrightarrow{v_s}$ in order to avoid the collision, as shown in Fig. 3(b). In this case, the optimal moving direction is selected from the set χ_0 (8), which is the set of all alternative directions. Hence, after the screening of the detection circle, the set of alternative directions can be expressed as

$$\chi_1 = \begin{cases} \chi_F, \, L_d - r_{ob} \geq r_d \\ \chi_0, \, L_d - r_{ob} < r_d. \end{cases} \tag{16}$$

It is noted that, the alternative directions in the set χ_1 cannot be guaranteed safe, i.e., the swarm may collide with the obstacle when moving in some of the moving directions selected from the set χ_1. The set χ_1 thus needs to be screened based on the function of the safety circle, in order to make sure that the optimal direction selected from the set is safe.

The function of the safety circle is shown in Fig. 3(c) and (d). The safety circle is defined to be inside the detection circle, since the safety circle takes effect after the set χ_0 is screened based on the function of the detection circle. The elimination of the moving directions depends on the comparison between the values of L_f, i.e., the distance between the corresponding predictive swarm and the obstacle, and d_f, i.e., the safety distance indicated in Fig. 3. If the obstacle enters the detection circle but locates outside the safety circle, as shown in Fig. 3(c), the direction from the swarm toward the obstacle (i.e., $\overrightarrow{v_{s1}}$) can be safe, because L_f is larger than d_f. In this case, the set of alternative directions is still χ_1, i.e., none of the alternative directions in the set χ_1 will be eliminated. However, when the obstacle enters the safety circle, as shown in Fig. 3(d), the moving direction from the swarm toward the obstacle (i.e., $\overrightarrow{v_{s1}}$) and some other directions in the set χ_1 need to be eliminated due to the low safety (i.e., $L_f < d_f$), as shown by the dashed orange arrows in Fig. 3(d). Then, the moving direction needs to change from $\overrightarrow{v_{s1}}$ to $\overrightarrow{v_{s2}}$. Hence, after the screening based on the functions of the detection circle and the safety circle, the set of alternative directions can be expressed as

$$\chi_2 = \begin{cases} \chi_1, L_d - r_{ob} \geq r_f \\ \{\theta \in \chi_1 \,|L_f \geq d_f \}, L_d - r_{ob} < r_f \end{cases} \tag{17}$$

where L_d is the distance between the current swarm center and the obstacle center.

As a result, the set χ_0 includes all possible alternative directions of the swarm locomotion. After the screening based on the functions of the detection circle and the safety circle, the initial set χ_0 is degenerated into the set χ_2. Moreover, by using the selection function in (9), the optimal moving direction of the swarm is selected from the set χ_2. It is noted that, for the obstacle that is not circular, when the distance between the swarm center and the edge of the obstacle is smaller than the radii of the circles, it can be regarded that the obstacle enters the circles.

C. Radius Control of Safety Circles

The safety circle is used to eliminate the unsafe alternative directions. When the safety circle is small, the safety distance d_f also reduces (7). When the obstacle enters the safety circle, the set χ_2 (17) will contain more alternative directions that meet the condition $L_f \geq d_f$. In this case, a large proportion of the alternative directions with a small direction deviation α remain, which leads to a low avoidance cost and a high avoidance efficiency. Therefore, the radius of the safety circle needs to be controlled based on the relative position between the swarm and obstacles, in order to simultaneously achieve obstacle avoidance and a high avoidance efficiency. Herein, the model predictive control (MPC) is applied to tune the radius of the safety circle.

We assume that when the swarm is avoiding the dynamic obstacle, the obstacle has a tendency of colliding with the swarm. In the line between the obstacle and the swarm, as shown by $\overrightarrow{O_{ob}O_s}$ in Fig. 3(c) and (d), the velocity component of the obstacle related to that of the swarm is assumed by $\boldsymbol{v}_r$, and $\overrightarrow{v_r}$ points from the obstacle toward the swarm. The Euclidean norm of the velocity component is $\|\boldsymbol{v}_r\|$. In this case, after a time t_{as}, the distance between the swarm and the obstacle will decrease $\|\boldsymbol{v}_r\| \cdot t_{as}$. We set the upper limit of the radius of the safety circle to r_{f0}, and the current radius of the safety circle can be expressed as

$$r_f = r_{f0} - \|\boldsymbol{v}_r\|\, t_{as}. \tag{18}$$

The assumed velocity component $\boldsymbol{v}_r$ depends on the distance between the swarm and the obstacle, and MPC method is adopted to obtain the optimal $\boldsymbol{v}_r$. Under the assumption, in the line between the swarm and the obstacle, the model of the relative motion between the swarm and the dynamic obstacle can be expressed as

$$\begin{bmatrix}\dot{\tilde{a}}(t)\\ \dot{\tilde{b}}(t)\end{bmatrix} = \begin{bmatrix}\cos(\theta_r) & -\|\boldsymbol{v}_r\|_{\max}\sin(\theta_r)\\ \sin(\theta_r) & \|\boldsymbol{v}_r\|_{\max}\cos(\theta_r)\end{bmatrix}\begin{bmatrix}\|\boldsymbol{v}_r(t)\|\\ \theta_r(t)\end{bmatrix} \tag{19}$$

where $[\dot{\tilde{a}}(t), \dot{\tilde{b}}(t)]^T$ is the vector of the obstacle velocity component related to that of the swarm in the line, $\dot{\tilde{a}}(t)$ and $\dot{\tilde{b}}(t)$ are its *x*-axis component and *y*-axis component, respectively. The direction from the obstacle center to the swarm center is θ_r, i.e., the angle between $\overrightarrow{O_{ob}O_s}$ and the positive *x*-axis. The assumed velocity of the obstacle is $\boldsymbol{v}_r(t)$, and $\|\boldsymbol{v}_r\|_{\max}$ is the upper limit of $\|\boldsymbol{v}_r(t)\|$. The state space of the model (19) in discrete time is

$$x(k+1) = Ax(k) + Bu(k) \tag{20}$$

where

$$x = \begin{bmatrix}\tilde{a}(t)\\ \tilde{b}(t)\end{bmatrix}, u = \begin{bmatrix}\|\boldsymbol{v}_r(t)\|\\ \theta_r(t)\end{bmatrix}$$

$$A = \begin{bmatrix}1 & 0\\ 0 & 1\end{bmatrix}, B = \begin{bmatrix}T\cos(\theta_r) & -T\|\boldsymbol{v}_r\|_{\max}\sin(\theta_r)\\ T\sin(\theta_r) & T\|\boldsymbol{v}_r\|_{\max}\cos(\theta_r)\end{bmatrix}. \tag{21}$$

The sampling time is *T*, and $[\tilde{a}(t), \tilde{b}(t)]^T$ is the position of the obstacle relative to the swarm.

The constraints are expressed as

$$\|\boldsymbol{v}_r(t)\| \cdot T < d_{so} \tag{22}$$

where d_{so} is the distance between the swarm and the obstacle.

In this case, the control objective is to find the optimal $\|\boldsymbol{v}_r(t)\|$ (i.e., $\|\boldsymbol{v}_{\text{ropt}}(t)\|$) that minimizes the following cost function:

$$J = \sum_{i=0}^{N} \left(x(k+i|k)^T Q x(k+i|k) + u(k+i|k)^T R u(k+i|k)\right) \tag{23}$$

where *N* is the prediction time domain, *k* is the current time, $x(k+i|k)$ and $u(k+i|k)$ are the predicted state and input based on the current state and input at time *k*, and *Q* and *R* are the weight matrices of collision and avoidance possibility, respectively.

After the optimization, the radius of the safety circle can be expressed as

$$r_f = r_{f0} - \|\boldsymbol{v}_{\text{ropt}}(t)\|\, t_{as}. \tag{24}$$

The $\|\boldsymbol{v}_{\text{ropt}}(t)\|$ changes based on the distance between the obstacle and the swarm, and the radius of the safety circle r_f thus changes accordingly. We also expect that the changing speed of r_f increases when the velocity of the dynamic obstacle increases.

D. Control Diagram of the System

The diagram of the control system is shown in Fig. 4. The system mainly consists of three units, i.e., a detection unit, an actuation unit, and a radar-based controller. The real-time images of the microrobotic swarm, the target, the boundaries, and the obstacles are observed by the optical microscope, in order to obtain the swarm position, the swarm radius, the target position, and the positions and radii of dynamic obstacles. The position and radius of the swarm are then input to the radar-based controller to generate the hierarchical radar. The positions and radii of dynamic obstacles are known for the controller. Meanwhile, the boundaries and target position are input to the global path planner to generate an initial path guiding the swarm between the boundaries. Subsequently, the waypoints in the path $(n_1, n_2 \ldots n_k)$ acting as phased goals are generated and taken into consideration for the optimal direction selection. Based on the set χ_2, the waypoints, and the positions of dynamic obstacles and the predictive swarms, the optimal moving direction θ_{opt} of the swarm is selected. Finally, the desired magnetic field can be obtained and generated to actuate and control the swarm.

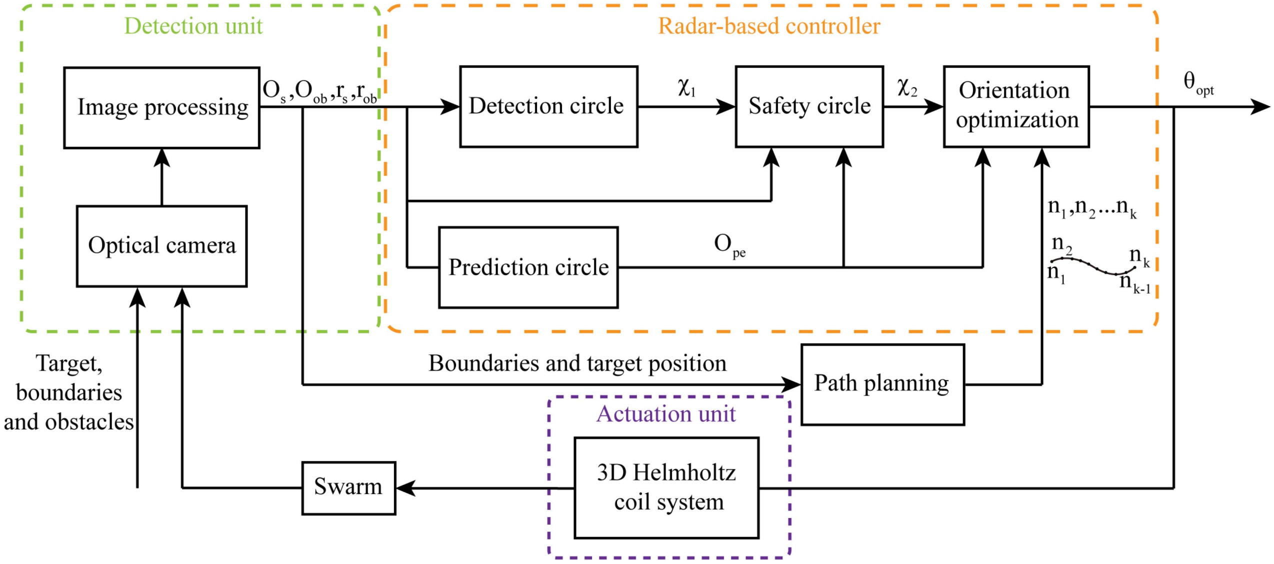

Fig. 4. Diagram of the control system. The system consists of a detection unit, an actuation unit and a radar-based controller. The input of the system are the swarm, the target, the boundaries, and the obstacles. The output is the optimal swarm moving direction θ_{opt}. The centers of the swarm, the predictive swarm, and the obstacle are O_s, O_{pe}, and O_{ob}, respectively. The radii of the swarm and the obstacle are r_s and r_{ob}, respectively. The set of the alternative directions after screened by the functions of the detection circle and the safety circle are χ_1 and χ_2, respectively. The waypoints in the global path are $n_1, n_2 \ldots n_k$.

IV. SIMULATION

A. Avoidance of a Single Dynamic Obstacle

Herein, the process that a swarm avoids a single dynamic obstacle utilizing the hierarchical radar with different radii of the detection and safety circles is simulated, as shown in Fig. 5, in order to explain the influence of the radii of the detection and safety circles on the control procedure. The influence of changing the radius of the prediction circle is not investigated, because the radius of the prediction circle is small (not larger than 0.625 body lengths of the swarm) and has little space to change, as shown in Section III-A. In simulations, the radius of the prediction circle is set to 125 pixels (0.625 body lengths of the swarm), as shown by the red circle.

In the simulation, a single obstacle moving downward with a fixed velocity is applied. In Case I, as shown in Fig. 5(a), a detection circle (i.e., the brown circle) with a small radius (i.e., 170 pixels) and a safety circle (i.e., the orange circle) with a small radius (i.e., 150 pixels) are defined in the hierarchical radar. The initial positions of the swarm P_0 and the dynamic obstacle is shown at $t = 0$ s, and at this moment, the moving direction of the swarm (i.e., the orange arrow) points from its center toward the target since the obstacle is out of the detection circle. The swarm keeps moving in the direction until $t = 12.1$ s, from P_0 to P_1. At the same time, the avoidance cost keeps as 0, as shown in Fig. 6(a). At $t = 12.1$ s, the dynamic obstacle enters the detection circle, and the avoidance behavior is triggered. The moving direction of the swarm changes in order to avoid the collision, while the avoidance cost starts increasing, as shown in Fig. 6(a). During avoidance, for instance, as shown at $t = 28$ s, the obstacle overlaps with the safety circle, and thus, the safety circle dominates the avoidance procedure. Due to the small radius of the safety circle, a large proportion of alternative directions with a small direction deviation α can be remained, which leads to a low avoidance cost [shown in Fig. 6(a)] and a high avoidance efficiency. Subsequently, the obstacle leaves the detection circle at $t = 30.6$ s, indicating the avoidance task is finished, and the swarm again moves toward the target straightly. During obstacle avoidance, the change of avoidance cost δ is shown in Fig. 6(a), and it comes to 0 again when the avoidance task is finished. Finally, at $t = 48.8$ s, the swarm reaches the target, and the approximate moving path of the swarm in the whole process is denoted by $P_0P_1P_2P_3P_4$, as shown in Fig. 5(a). The time duration when the swarm is avoiding the obstacle, i.e., the period when the obstacle is overlapping with the detection circle (from $t = 12.1$ s to $t = 30.6$ s), is denoted by t_a. The total time of the swarm moving from the starting point to the target is denoted by t_f. Due to the small detection circle, t_a is small (i.e., $t_a = 18.5$ s). In this case, the time period when the obstacle is out of the detection circle, i.e., $t_f - t_a$ is long. During the period, the avoidance cost $\delta = 0$, and it leads to a small average avoidance cost $\overline{\delta}$ of the whole process. As a result, due to the small safety circle and the small detection circle, the average avoidance cost $\overline{\delta} = 0.14$, the total time $t_f = 48.8$ s and the avoidance time $t_a = 18.5$ s are the smallest among the three cases.

In Case II, a detection circle with a radius of 350 pixels and a safety circle with a radius of 150 pixels are defined in the hierarchical radar, in order to explain the influence of the detection circle radius on the control procedure, as shown in Fig. 5(b). The initial positions of the swarm and the obstacle are shown at $t = 0$ s, which are the same as those in Case I. At the beginning (i.e., $t = 0$ s), the swarm moves toward the target since the obstacle is not detected. However, compared to Case I, the obstacle enters the detection circle earlier (i.e., $t = 7.9$ s) due to the larger detection circle, and the avoidance cost becomes larger than 0 at $t = 7.9$ s, as shown in Fig. 6(b). During avoidance, at $t = 28$ s, the obstacle overlaps with the detection circle not the safety circle due to the large distance between the safety circle

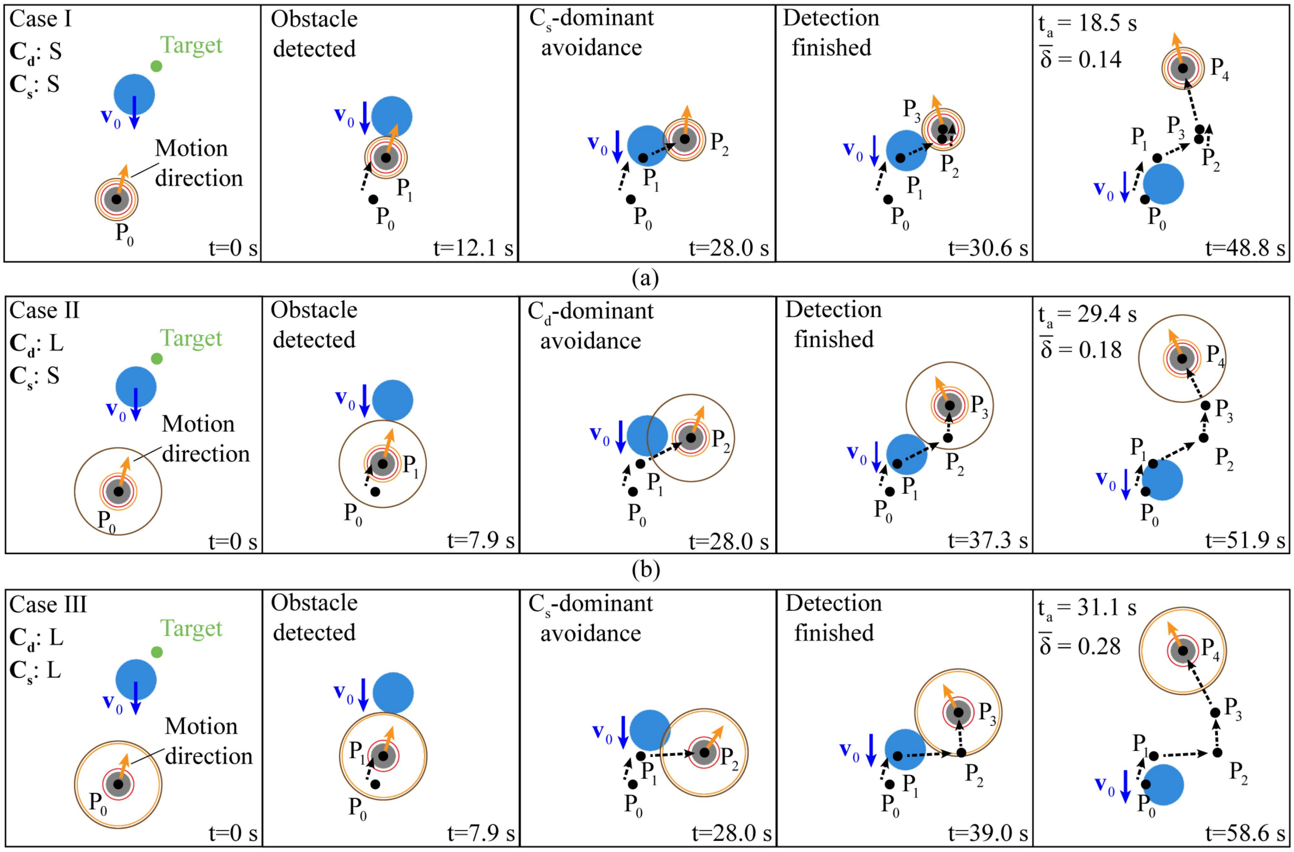

(a)

(b)

(c)

Fig. 5. Simulation results of avoidance of a dynamic obstacle in the three cases. (a) Case I: A small detection circle and a small safety circle. (b) Case II: A large detection circle and a small safety circle. (c) Case III: A large detection circle and a large safety circle. The grey and blue circles indicate the swarm and the obstacle, respectively. The green dot denotes the target. The brown, orange, and red circles are the detection (C_d), safety (C_s), and prediction circle (C_p), respectively. The orange and blue arrows indicate the velocity of the swarm and the dynamic obstacle, respectively. The black dashed arrows indicate the approximate moving path of the swarm. L represents a relatively large size, and S indicates a relatively small size.

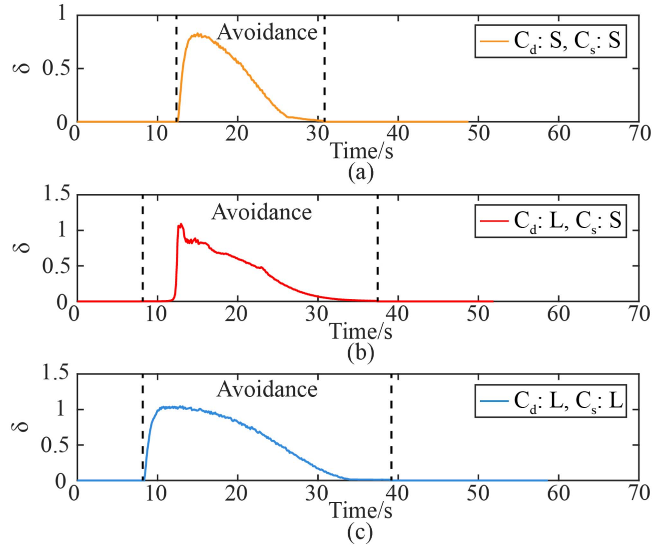

(a)

(b)

(c)

Fig. 6. Avoidance cost δ in the three cases. (a) The avoidance cost in Case I. (b) The avoidance cost in Case II. (c) The avoidance cost in Case III. The detection circle and the safety circle are C_d and C_s, respectively. L represents a relatively large size, and S indicates a relatively small size.

and the detection circle, and thus, the detection circle dominates the avoidance procedure. Due to the larger detection circle, the avoidance weight q_a increases (10). Therefore, when selecting the optimal direction, the term $q_a N(\|{}^i\overrightarrow{O_{pe}O_{ob}}\| - r_s - r_{ob})$ in (9) relating to the dynamic obstacle avoidance will be higher. As a result, in the control procedure, the swarm has a higher tendency of avoiding the obstacle, and the direction deviation α is larger compared to that in Fig. 5(a), which results in a higher avoidance cost and a lower avoidance efficiency. Subsequently, the obstacle leaves the detection circle at $t = 37.3$ s and reaches the target at $t = 51.9$ s, as shown in Fig. 5(b). Due to the larger detection circle, $t_a = 29.4$ s is larger compared to that in case I (i.e., $t_a = 18.5$ s), and the time period that the moving direction of the swarm is influenced by the obstacle is longer, leading to a higher avoidance cost. As a result, the average avoidance cost $\overline{\delta} = 0.18$, total time $t_f = 51.9$ s, and avoidance time $t_a = 29.4$ s are larger than those in Case I.

Subsequently, in Case III, a detection circle with a radius of 350 pixels and a safety circle with a radius of 330 pixels are defined in the hierarchical radar, in order to explain the influence of the safety circle radius on the control procedure, as shown in

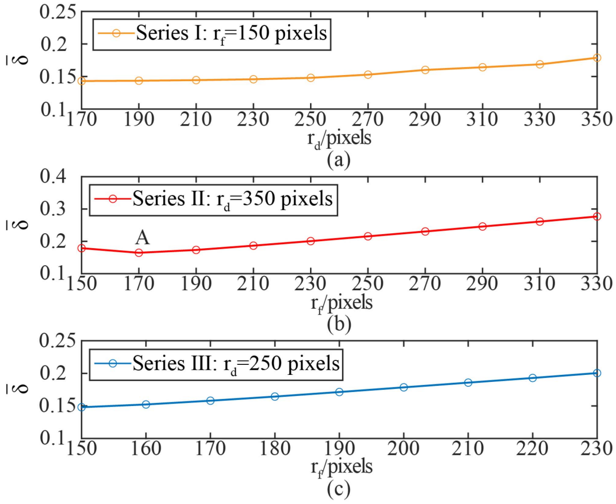

Fig. 7. Average avoidance cost $\bar{\delta}$ in three series of simulations. (a) The average avoidance cost $\bar{\delta}$ in series I: r_d ranges from 170 pixels to 350 pixels while r_f remains at 150 pixels. (b) The average avoidance cost $\bar{\delta}$ in series II: r_f ranges from 150 pixels to 330 pixels while r_d remains at 350 pixels. (c) The average avoidance cost $\bar{\delta}$ in Series III: r_f ranges from 150 pixels to 230 pixels while r_d remains at 250 pixels.

Fig. 5(c). All other initial conditions are maintained the same with those in Case I and Case II. At $t = 28$ s, due to the large safety circle and the small distance between the safety circle and the detection circle, the obstacle enters the safety circle, and thus, the safety circle dominates the avoidance procedure. In this case, more moving directions that have a small direction deviation α are eliminated, and the avoidance cost will thus be higher compared to that in Case II, which leads to a lower avoidance efficiency. Subsequently, the obstacle leaves the detection circle at $t = 39.0$ s and reaches the target at $t = 58.6$ s, as shown in Fig. 5(c). The minor difference between t_a in Case III (i.e., 31.1 s) and that in Case II (i.e., 29.4 s) is observed, due to the same radii of the detection circles in the two cases. As a result, due to the largest radii of the safety circle and the detection circle, the average avoidance cost $\bar{\delta} = 0.28$ and the total time $t_f = 58.6$ s are largest among three cases.

The curves of the avoidance cost δ in the three cases are shown in Fig. 6. When the swarm starts avoiding the obstacle, the avoidance cost first increases, due to the growing influence of the obstacle on the swarm when the obstacle is approaching the swarm. Subsequently, the avoidance cost decreases, because the swarm completes the avoidance and gradually leaves the obstacle, leading to a decreasing influence of the obstacle on the swarm. From Fig. 6, the avoidance time t_a, the total time t_f are the shortest in Case I, and the average/maximum avoidance cost in Case I is also the smallest one in the three cases.

To test statistically on how radii values of the detection and safety circle impact the avoidance cost, we have conducted more simulations to compare the average avoidance cost from the starting point to the target with different radii values, and the result is shown in Fig. 7. The initial conditions of each simulation are the same as those in Cases I–III. We have divided the simulations into three series as follows.

Series I: The average avoidance cost when the radius of the detection circle is different (i.e., from 170 pixels to 350 pixels), and the radius of the safety circle remains the same (i.e., 150 pixels).

Series II: The average avoidance cost when the radius of the safety circle is different (i.e., from 150 pixels to 330 pixels), and the radius of the detection circle remains the same (i.e., 350 pixels).

Series III: The average avoidance cost when the radius of the safety circle is different (i.e., from 150 pixels to 230 pixels), and the radius of the detection circle remains the same (i.e., 250 pixels).

In Series I, when the radius of the safety circle remains the same, the average avoidance cost increases as the detection circle is larger. This is because when the detection circle is larger, the avoidance weight q_a when selecting the optimal direction is larger (10), which leads to a larger direction deviation α and increases the avoidance cost. In addition, a larger detection circle will lead to a longer avoidance time, which also increases the avoidance cost.

In Series II, the radius of the detection circle remains the same. The average avoidance cost increases with the radius of the safety circle, when the radius of the safety circle is larger than 170 pixels, please refer to the point A in Fig. 7. This is because when the safety circle is larger, more alternative directions with a small α will be eliminated, which increases the average avoidance cost. When the radius of the safety circle is smaller than 170 pixels, the avoidance cost decreases with the radius of the safety circle, please refer to the point A in Fig. 7. The reason is that when the safety circle is smaller, the distance between the obstacle and the swarm decreases, and the avoidance weight q_a increases (10), which leads to a higher avoidance cost. If the influence of the high avoidance weight on the avoidance cost is larger than that of the small radius of the safety circle, the avoidance cost will increase. However, in experiments, the radius of the detection circle is smaller than that in series II (i.e., 350 pixels). If the radius of the detection circle is small, e.g., 250 pixels, the influence of the avoidance weight q_a will be lower than that caused by the radius of the safety circle (10). In this case, the avoidance cost will increase when the radius of the safety circle is larger, as shown in Series III.

From Cases I–III and Series I–III, we can obtain the conclusion that, to decrease the avoidance cost δ, the detection circle and the safety circle need to be designed small. In fact, the radii of the detection circle and the safety circle have a lower limitation, e.g., 0.55 body lengths of the swarm, in order to leave the swarm with sufficient time to respond to the obstacles for collision avoidance.

B. Avoidance of Multiple Dynamic Obstacles

To better validate the effectiveness of the radar-based algorithm, 12 moving obstacles with different velocities and initial positions are applied, as shown in Fig. 8(a). A hierarchical radar with a detection circle (i.e., the brown circle), a safety circle (i.e., the orange circle), and a prediction circle (i.e., the red circle) is applied. The radius of the prediction circle is 125 pixels (0.625

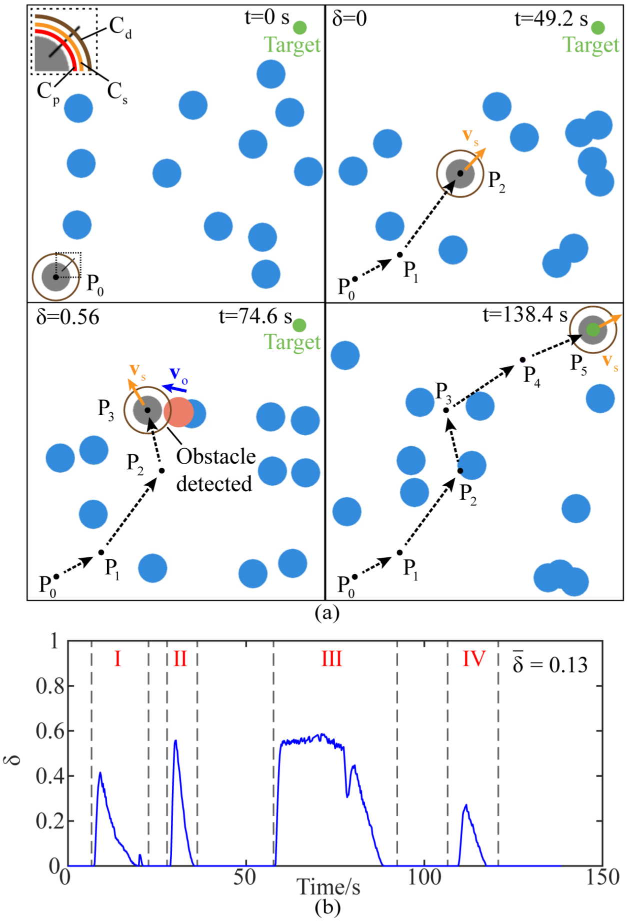

Fig. 8. Simulation results of the avoidance of multiple moving obstacles. (a) The simulated procedure of a swarm avoiding multiple moving obstacles. (b) The avoidance cost δ in the simulation. The grey and blue circles indicate the swarm and the obstacle, respectively. The obstacle overlapping with the detection circle is highlighted with light red color. The green dot is the target. The brown, orange, and red circles are the detection (C_d), safety (C_s), and prediction circle (C_p), respectively. The orange and blue arrows indicate the velocity of the swarm and the dynamic obstacle, respectively. The black dashed arrows indicate the approximate moving path of the swarm. Time periods I–IV are those when the swarm is performing the avoidance task.

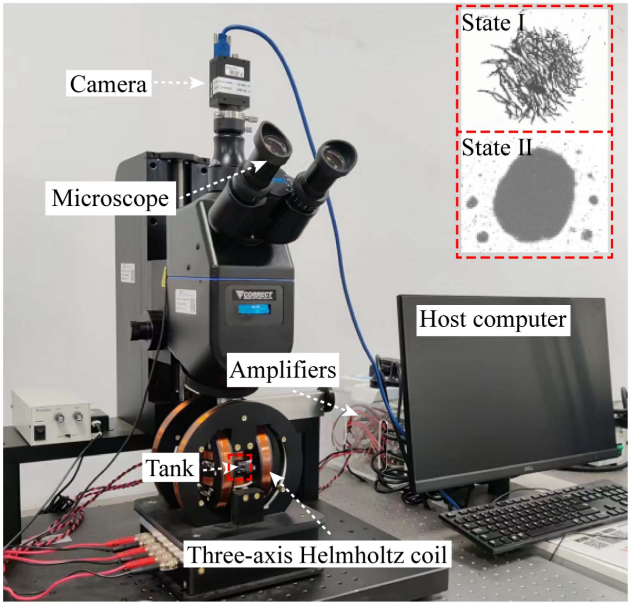

Fig. 9. Experimental system. The insets show the experimental images of two states of nanoparticles. State I: Dispersed nanoparticle clusters. State II: A swarm.

body lengths of the swarm). To decrease the avoidance cost, a detection circle with a small radius (i.e., 150 pixels) is defined, and the upper limit of the radius of the safety circle is set to 150 pixels, which is the same as the radius of the detection circle. Using the MPC strategy introduced in Section III-C, the radius of the safety circle is

$$r_f = 150 - \left\| \boldsymbol{v}_{\text{ropt}}(t) \right\| . \tag{25}$$

The radius of the safety circle can change automatically according to the distance between the obstacle and the swarm.

The initial positions of the swarm and dynamic obstacles are shown at $t = 0$ s. When there is no obstacle overlapping with the detection circle, the avoidance behavior is not triggered, and the moving direction of the swarm is toward the target, as shown at $t = 49.2$ s in Fig. 8(a). When an obstacle enters the detection circle, the swarm will try to avoid it (i.e., the light red circle), as shown at $t = 74.6$ s. The avoidance cost δ is 0.56 at $t = 74.6$ s, indicating a low avoidance efficiency at the moment. The swarm reaches the target at $t = 138.4$ s.

The curve of the real-time avoidance cost δ is shown in Fig. 8(b). There are several time periods when δ is 0, indicating no avoidance is performed, because dynamic obstacles are out of the detection circle. In addition, the time periods when the swarm is avoiding the obstacle can also be observed, as shown by the time period I to the time period IV in Fig. 8(b). The average avoidance cost $\bar{\delta} = 0.13$ is low, which validates that the proposed strategy is effective for the swarm to avoid multiple moving obstacles.

V. EXPERIMENTAL RESULTS

A. System Setup

The magnetic actuation system is shown in Fig. 9. We use a three-axis Helmholtz coil to generate the rotating magnetic field for the actuation of microrobotic swarms, an optical microscope and a camera for vision feedback, along with a host computer to implement the control strategy. One drop of Fe_3O_4 nanoparticle suspension (20 μL, 1 mg/mL) is added into 5% PVP solution in the tank, and the diameter of the nanoparticle is 100 nm. Using the rotating magnetic field with a frequency of 16 Hz and a strength of 8 mT, the dispersed magnetic nanoparticles form a vortex-like swarm, as shown in the insets in Fig. 9. Due to different initial particle concentrations and that inside the swarm after swarm formation, the diameter of the swarm can be different from case to case, and in addition, the diameter of the swarm also changes when moving due to the fluidic drags [42]. In the experiments, the diameter of the swarm ranges from 600 to 1000 μm. A silicon wafer is used as the substrate to enhance the imaging contrast. In the experiments, the computation time

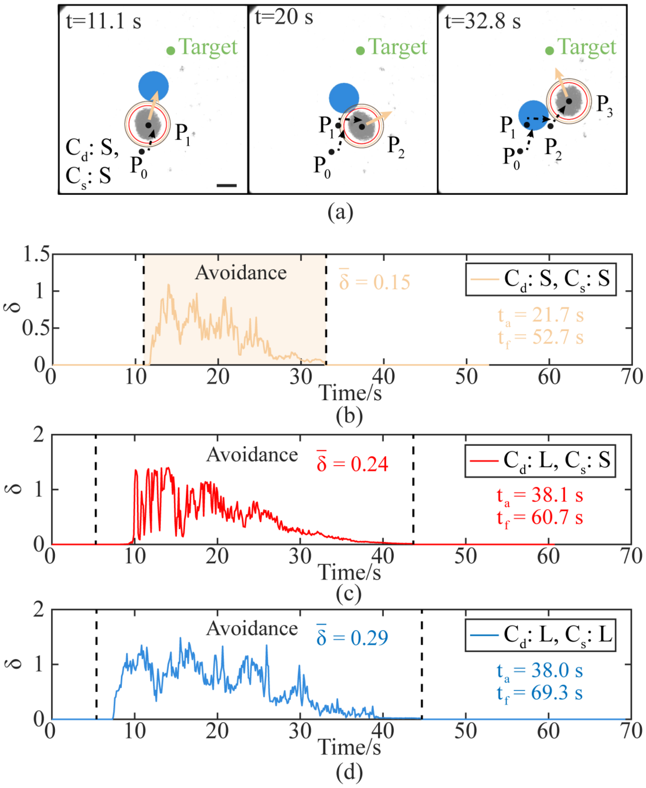

Fig. 10. Experimental validation of the avoidance of a dynamic obstacle with different detection and safety circles. (a) The experimental procedure of the avoidance in Case I. (b) The avoidance cost δ in Case I: A small detection circle and a small safety circle. In Case I, $d_p = 25$ pixels, $d_f = 25$ pixels, and $d_r = 70$ pixels. (c) The avoidance cost δ in Case II: A large detection circle and a small safety circle. In Case II, $d_p = 25$ pixels, $d_f = 25$ pixels, and $d_r = 250$ pixels. (d) The avoidance cost δ in Case III: A large detection circle and a large safety circle. In Case III, $d_p = 25$ pixels, $d_f = 205$ pixels, and $d_r = 250$ pixels. The blue circle and the green dot indicate the dynamic obstacle and the target, respectively. The brown, orange, and red circles are the detection (C_d), safety (C_s), and prediction circle (C_p), respectively. L represents a relatively large size, and S indicates a relatively small size. The scale bar is 500 μm.

of the image processing for visual feedback is 0.05 s, and the time response of the swarm to the magnetic field is 0.1 s. The dynamic obstacles are virtually overlaid on the real experiment's imaging plane. If the obstacle has a higher velocity than that of the swarm, and meanwhile, it has the tendency to collide with the swarm, the collision cannot be avoided. In this case, the velocity of the swarm is set higher than those of the obstacles in the experiments.

B. Avoidance of a Single Dynamic Obstacle

To validate the functions of the detection circle and the safety circle, the experimental results of the avoidance of a single dynamic obstacle are shown in Fig. 10. A single obstacle (i.e., the blue circle) moving downward with a fixed velocity of 40 μm/s is applied, and the velocity of the swarm is 106.4 μm/s. The diameter of the obstacle is 900 μm. Different detection circles and safety circles are defined in the hierarchical radar, i.e., Case I: a small detection circle and a small safety circle; Case II: a large detection circle and a small safety circle; Case III: a large detection circle and a large safety circle. Because in experiments, the radius of the swarm is not a constant value, the radii of the prediction circle $r_p(t)$, the safety circle $r_f(t)$, and the detection circle $r_d(t)$ are modified as

$$\begin{cases} r_p(t) = r_s(t) + d_p \\ r_f(t) = r_s(t) + d_p + d_f \\ r_d(t) = r_s(t) + d_r \end{cases} \tag{26}$$

where $r_s(t)$ is the changing radius of the swarm, and d_p, d_f, and d_r are the distance between the predictive swarm and the current swarm, the safety distance and the detection range, respectively.

The experimental procedure of the avoidance in Case I is shown in Fig. 10(a). At $t = 0$ s, the swarm is at position P_0, and at $t = 11.1$ s, the swarm moves to P_1. At the same time, the obstacle enters the detection circle, which triggers the avoidance behavior. Therefore, a significant increase of the avoidance cost δ is resulted in, as shown in Fig. 10(b). During avoidance, for instance, as shown at $t = 20$ s in Fig. 10(a), the obstacle overlaps with the safety circle, and the safety circle dominates the avoidance procedure. Due to the small radius of the safety circle, the direction deviation α is small, which leads to a low avoidance cost [shown in the colored region of Fig. 10(b)] and a high avoidance efficiency. Subsequently, the obstacle leaves the detection circle at $t = 32.8$ s, and the avoidance task is finished as shown in Fig. 10(a). Meanwhile, the avoidance cost comes to 0 again, as shown in Fig. 10(b).

The curves of the avoidance cost δ in Case I, Case II, and Case III are shown in Fig. 10(b), (c) and (d), respectively. The avoidance cost increases first then decreases, due to the changing influence of the dynamic obstacle on the swarm. In these three cases, with the increasing of the radii of the detection circle and the safety circle, the average avoidance cost $\bar{\delta}$ are 0.15, 0.24, and 0.29, respectively. The total time t_f thus increases significantly from Case I to Case III. As a result, the experimental results have a good agreement with the simulations. In addition, the updating frequency of the moving direction obtained from the control strategy is 9.6 Hz, which shows the high effectiveness of our proposed strategy.

The curves in the experiments shown in Fig. 10 have more oscillation compared to the curves in the simulation, as shown in Fig. 6. The reasons can be that, the radius of the swarm is changing, and oscillation exists when detecting the real-time distance between the swarm and the target.

C. Avoidance of Multiple Dynamic Obstacles

To validate the effectiveness of the radar-based algorithm in avoiding multiple dynamic obstacles, herein, 12 obstacles with random positions and velocities (i.e., the blue circles) are deployed, as shown in Fig. 11. The maximum velocity and the diameter of the obstacles are 66.8 μm/s and 550 μm, respectively. The velocity of the swarm in this case is 85.8 μm /s. The hierarchical radar is applied to navigate the swarm for collision avoidance. The precise values of $r_p(t)$, $r_d(t)$, and $r_f(t)$ cannot be obtained when multiple randomly moving obstacles exist. To control $r_p(t)$, $r_d(t)$, and $r_f(t)$ in ranges that can guarantee the

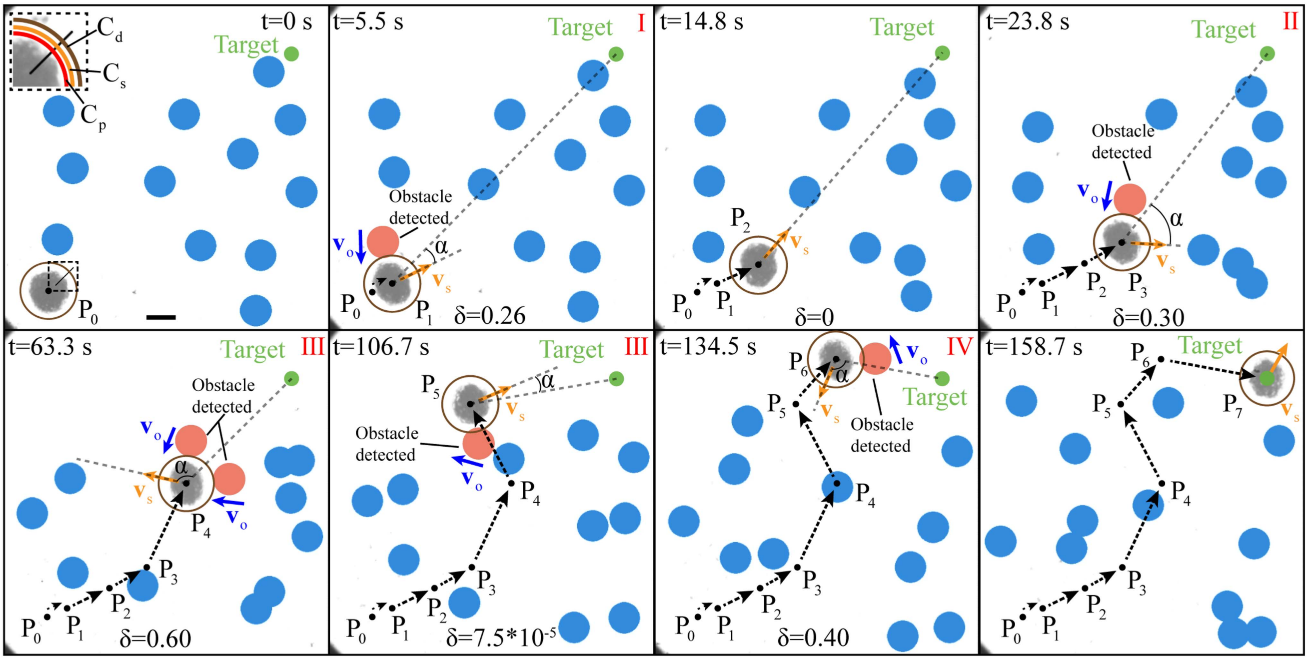

Fig. 11. Experimental results of the avoidance of multiple moving obstacles. The blue circles indicate the dynamic obstacles. The obstacle overlapping with the detection circle is highlighted with light red color. The green dot is the target. The brown, orange, and red circles are the detection (C_d), safety (C_s), and prediction circle (C_p), respectively. The orange and blue arrows indicate the velocity of the swarm and the dynamic obstacle, respectively. The black dashed arrows indicate the approximate moving path of the swarm. The dashed grey lines are the auxiliary lines to represent the direction deviation α. Time periods I–IV are those when the swarm is performing the avoidance task. The scale bar is 500 μm.

avoidance of collisions and improve the avoidance efficiency, based on preliminary simulation and experimental results, d_p, d_f, and d_r in (26) are set to 25, 25, and 50 pixels, respectively. In addition, the radius of the safety circle is further controlled using MPC based on (24). The radii of the prediction circle $r_p(t)$, the safety circle $r_f(t)$, and the detection circle $r_d(t)$ can then be expressed as

$$\begin{aligned} r_p(t) &= r_s(t) + 25 \\ r_f(t) &= r_s(t) + 50 - \|\boldsymbol{v}_{\text{ropt}}(t)\| \\ r_d(t) &= r_s(t) + 50 \end{aligned} \tag{27}$$

where $r_s(t)$ is the radius of the swarm.

The initial positions of the swarm and dynamic obstacles are shown at $t = 0$ s, and the initial position of the swarm is denoted by P_0. During the whole process, there are four time periods when there are obstacles overlapping with the detection circle (i.e., time period I–IV). When the swarm moves from P_0 to P_1 at $t = 5.5$ s in the time period I, the swarm is avoiding the dynamic obstacle overlapping with the detection circle (i.e., the light red circle), and the avoidance cost δ is 0.26 at $t = 5.5$ s. When there is no obstacle overlapping with the detection circle, the swarm is moving toward the target, and the avoidance cost $\delta = 0$, as shown at $t = 14.8$ s. At $t = 23.8$ s in the time period II, the second dynamic obstacle is overlapping with the detection circle. The avoidance cost $\delta = 0.30$ at $t = 23.8$ s is higher than that at $t = 5.5$ s (i.e., $\delta = 0.26$), because the direction deviation α [in (4)] is larger. Then, the swarm moves to P_4 at $t = 63.3$ s in time period III. At $t = 63.3$ s, two dynamic obstacles overlap with the detection circle, as shown by the light red circles, the swarm is triggered to avoid the nearer obstacle. At $t = 63.3$ s, since the distance between the swarm and the two dynamic obstacles is changing, the one near to the swarm is changing by turns, and both of them will have influence on the locomotion of the swarm. As a result, the moving direction of the swarm at $t = 63.3$ s points to the upper-left side in order to avoid the two dynamic obstacles, as shown by the orange arrow. The moving direction also leads to a large direction deviation α and a large avoidance cost $\delta = 0.60$. Subsequently, the swarm moves to P_5 at $t = 106.7$ s. From P_4 to P_5, one of the dynamic obstacles encountered by the swarm at $t = 63.3$ s leaves the detection circle, and the avoidance cost δ is small (i.e., $\delta = 7.5 * 10^{-5}$) at $t = 106.7$ s due to the small direction deviation α and the small distance between the swarm and the target. At $t = 134.5$ s in the time period IV, in order to avoid the upper boundary and the obstacle, the moving direction of the swarm points to the bottom-left, which leads to large direction deviation α and high avoidance cost (i.e., $\delta = 0.40$). Finally, at $t = 158.7$ s, the swarm reaches the target. The increase of the number of dynamic obstacles (i.e., from a single obstacle to twelve obstacles) leads to higher computation load. When twelve obstacles are deployed, the updating frequency of the moving direction obtained from the control strategy is 4.3 Hz, which is lower than that when only one obstacle is deployed in Section V-B (i.e., 9.6 Hz). Both of the updating frequencies are sufficient for the swarm to perform the avoidance task, which validates the effectiveness of our strategy.

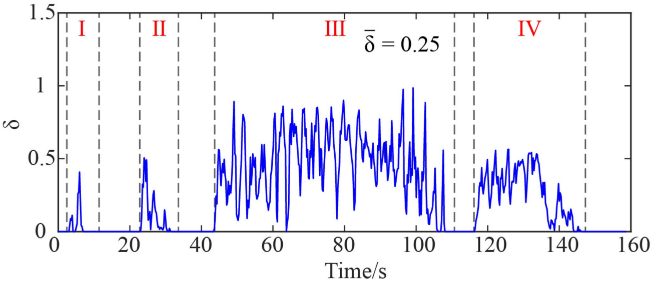

Fig. 12. Real-time avoidance cost δ during the avoidance procedure from multiple moving obstacles. Time periods I–IV are those when the swarm is performing the avoidance task.

The curve of avoidance cost δ in the whole process is shown in Fig. 12, and the four time periods when there are obstacles overlapping with the detection circle (i.e., time period I–IV) are labeled. The average distance between the swarm and the obstacle during the avoidance period is 75.31 μm (i.e., about 0.10 body lengths of the swarm). The successful avoidance of multiple moving obstacles with an average avoidance cost $\bar{\delta} = 0.25$ validates the effectiveness and high efficiency of the proposed control method.

D. Dynamic Obstacle Avoidance in a Micromaze

To further verify the effectiveness of the radar-based control strategy in a more complex environment, a micromaze and different types of dynamic obstacles are preset in the workspace, as shown in Fig. 13. An improved global path planner is combined with the modified radar-based algorithm to navigate the swarm to the target in the micromaze while avoiding dynamic obstacles. Modifications have been made to the radar-based algorithm, in order to adapt to different obstacles. As shown in Fig. 13(a), a global path from the original point to the target is generated by the path planner, in order to navigate the swarm in the micromaze without obstacles. Herein, we use the fast marching tree algorithm (FMT*) [46] to generate the global path. To prevent collisions between the swarm and the walls of the micromaze, we consider the radius of the swarm. The constraint of the sampling points can be expressed as

$$0 < \text{Dist}(\text{node}, \text{wall}) < r_{s\max} \tag{28}$$

where $r_{s\max}$ is the maximum radius of the swarm, and Dist(node, wall) is the distance between the sampling points and the walls.

Using the proposed algorithm, the tree branches between sampling points (i.e., the green lines) have a distance between the walls, as shown in Fig. 13(a). Based on the FMT*, a global path is generated by linking the chosen sampling points (i.e., the red line), and the global path will keep a predefined distance between the walls, ensuring the avoidance of collisions between the swarm and walls. The waypoints in the global path are n_1(original point), $n_2, \ldots n_9, n_{10}$(target), as shown by the red dots. The waypoints act as phased goals to navigate the swarm and will be reached by the swarm in sequence, from n_1 to n_{10}.

Herein, three types of dynamic obstacles are applied, i.e., moving obstacles, reversibly expanding obstacles, and valve-like obstacles, as shown in Fig. 13(b). The moving obstacles in the left side of the maze have a diameter of 330 μm, and they perform 1-D harmonic motion with a maximum velocity of 30 μm/s. The moving obstacles in the right side of the maze with a diameter of 360 μm perform harmonic motion along two curves in the same circle with opposite velocities, and the maximum velocity is 10 μm/s. The diameter of the reversibly expanding obstacle ranges from 140 to 800 μm. The motion of the valve-like obstacles (i.e., the orange rectangles) changes width of the space in between from 0 to 1485 μm. The velocity of the swarm in this case is 85.8 μm /s.

From $t = 0$ s to $t = 31.6$ s, the swarm moves from P_0 to P_1, and the phased goal changes from n_1 to n_3. The swarm avoids one of the moving obstacles using the proposed algorithm at $t = 31.6$ s, as shown in Fig. 13(c). At t = 67.1 s, the valve-like obstacle closes, and the velocity controller stops the swarm to wait for the reopening, as shown in Fig. 13(d). The velocity control for the valve-like obstacle avoidance can be expressed as

$$\boldsymbol{v}_s = \begin{cases} 0, & A = 0, d(t) < D \\ \boldsymbol{v}_s, & \text{others} \end{cases} \tag{29}$$

where A is the area surrounding the valve-like obstacle (i.e., the grey dashed rectangle). If the swarm enters the area A, $A = 0$. The width of the space in the valve-like obstacle is $d(t)$, and if $d(t)$ is less than the threshold D when $A = 0$, the swarm will stop moving (i.e., $\boldsymbol{v}_s = 0$), as shown in Fig. 13(d).

After the space between the valve-like obstacle expands larger than the swarm size, the swarm crosses the valve, as shown in Fig. 13(e). The strategy of avoiding the rectangular obstacle can be expressed as

$$\text{Dist}(P_e, b_r) < r_s(t) + d_f \tag{30}$$

where P_e is the position of the predictive swarm in the hierarchical radar, b_r, $r_s(t)$, and d_f are boundaries of the rectangles, the radius of the swarm, and the safety distance, respectively. Based on (30), the alternative directions that are unsafe for rectangular obstacle avoidance are eliminated, and the valve-like obstacle can be avoided using the strategy.

To avoid the reversibly expanding obstacle, the selection function in (9) is modified to

$$\phi_i = q_t N\left(\frac{1}{\left\|\overrightarrow{{}^{i}O_{pe}O_t}\right\|}\right) + q_a N\left(\left\|\overrightarrow{{}^{i}O_{pe}O_{ob}}\right\| - r_s - r_{ob}(t)\right). \tag{31}$$

In addition, the walls of the micromaze are also regarded as rectangular obstacles. The swarm can thus avoid the wall of the micromaze and the reversibly expanding obstacle simultaneously, at $t = 162.4$ s, as shown in Fig. 13(f).

At t = 332.6 s, the swarm avoids the valve-like obstacle again using the strategy shown in (29) and (30), as presented in Fig. 13(g). Finally, at t = 408.2 s, the swarm reaches the target, as shown in Fig. 13(h). Due to the influence of dynamic obstacles, the approximate moving path of the swarm (i.e.,

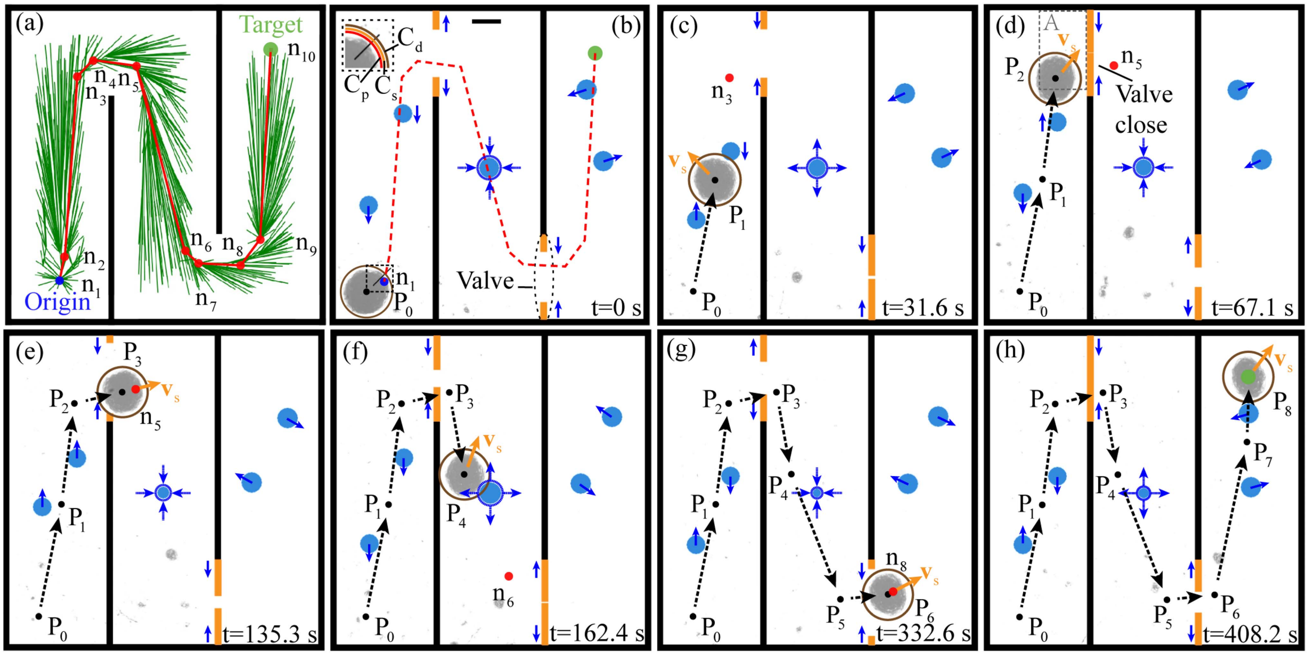

Fig. 13. Experimental results of global path generation and targeted locomotion of a swarm while avoiding different types of dynamic obstacles in a micromaze. (a) The global path generated by the fast marching tree algorithm. (b)–(h) The experimental results of navigation of a swarm while avoiding different types of dynamic obstacles in a micromaze. The red and red dashed lines represent the global path in the micromaze. The green lines represent the tree branches. The blue and red dots are the original point and waypoints of the path, respectively. The green dot denotes the target. The blue circles on both sides and in the middle represent moving obstacles and the reversibly expanding obstacle, respectively. The orange rectangles are the valve-like obstacles. The grey dashed rectangle indicates the area surrounding the valve-like obstacle. The brown, orange, and red circles are the detection (C_d), safety (C_s), and prediction circle (C_p), respectively. The orange arrow indicates the velocity of the swarm. The blue arrows indicate the moving direction or the deformation direction of the dynamic obstacles. The black dashed arrows indicate the approximate moving path of the swarm. In this case, d_p, d_f, and d_r are set to 25, 25, and 50 pixels, respectively. The scale bar is 500 μm.

$P_0, P_1 \ldots P_7, P_8$) is modified locally, which comes to be different from the initial global path (i.e., the red dashed line). The experimental results validate the effectiveness of our strategy in avoiding different kinds of obstacles in a micromaze.

VI. CONCLUSION

In this article, we proposed a radar-based control algorithm for dynamic obstacle avoidance using a microrobotic swarm. Based on the position and size of the swarm captured through imaging feedback, the hierarchical radar is generated. The detection circle, the safety circle, and the prediction circle of the radar cooperate to select the optimal moving direction of the swarm. We also proposed a criterion to evaluate the real-time locomotion efficiency during dynamic obstacle avoidance, i.e., the avoidance efficiency. Combined with the visual feedback, the swarm can be controlled to move to predefined targets with the interference of multiple dynamic obstacles. With the global path planner, the swarm can reach the target in a micromaze while avoiding different types of dynamic obstacles successfully. This work carries fundamental interest in the motion control of microrobots, and provides a prototypical paradigm for the effective control of microrobotic swarms for collision avoidance. It sheds light on the adaptive navigation of active matters in complex and dynamic environments. The proposed strategy has the potential to be used in 3-D dynamic obstacle avoidance by converting the 2-D hierarchical radar into a 3-D hierarchical radar.

ACKNOWLEDGMENT

The authors would like to thank Junhui Law (University of Toronto) and Huimin Zhang (The Chinese University of Hong Kong, Shenzhen) for fruitful discussions.

REFERENCES

[1] B. J. Nelson, I. K. Kaliakatsos, and J. J. Abbott, "Microrobots for minimally invasive medicine," *Annu. Rev. Biomed. Eng.*, vol. 12, pp. 55–85, 2010.

[2] X. Yan et al., "Multifunctional biohybrid magnetite microrobots for imaging-guided therapy," *Sci. Robot.*, vol. 2, no. 12, 2017, Art. no. eaaq1155.

[3] J. Li, B. E.-F. de Ávila, W. Gao, L. Zhang, and J. Wang, "Micro/nanorobots for biomedicine: Delivery, surgery, sensing, and detoxification," *Sci. Robot.*, vol. 2, no. 4, 2017, Art. no. eaam6431.

[4] M. Sitti et al., "Biomedical applications of untethered mobile milli/microrobots," *Proc. IEEE*, vol. 103, no. 2, pp. 205–224, Feb. 2015.

[5] X. Yang et al., "An agglutinate magnetic spray transforms inanimate objects into millirobots for biomedical applications," *Sci. Robot.*, vol. 5, no. 48, 2020, Art. no. eabc8191.

[6] Z. Zheng et al., "Ionic shape-morphing microrobotic end-effectors for environmentally adaptive targeting, releasing, and sampling," *Nature Commun.*, vol. 12, no. 1, 2021, Art. no. 1598.

[7] X. Li et al., "Holographic display-based control for high-accuracy photolithography of cellular micro-scaffold with heterogeneous architecture," *IEEE/ASME Trans. Mechatron.*, vol. 27, no. 2, pp. 1117–1127, Apr. 2021.

[8] J. Cui, H. Wang, Q. Shi, and T. Sun, "Pulsed microfluid force-based on-chip modular fabrication for liver lobule-like 3D cellular models," *Cyborg Bionic Syst.*, vol. 2021, 2021, Art. no. 9871396.

[9] Y. Hu, "Self-assembly of DNA molecules: Towards DNA nanorobots for biomedical applications," *Cyborg Bionic Syst.*, vol. 2021, 2021, Art. no. 9807520.

[10] L. Zhang, J. J. Abbott, L. Dong, B. E. Kratochvil, D. Bell, and B. J. Nelson, “Artificial bacterial flagella: Fabrication and magnetic control,” *Appl. Phys. Lett.*, vol. 94, no. 6, 2009, Art. no. 064107.

[11] S. Jeon, J. Nam, W. Lee, and G. Jang, “Selective navigating and unclogging motions of an intravascular helical magnetic millirobot actuated by external biaxial rotating magnetic fields,” *IEEE/ASME Trans. Mechatron.*, vol. 22, no. 3, pp. 1456–1464, Jun. 2017.

[12] X. Yan et al., “Magnetite nanostructured porous hollow helical microswimmers for targeted delivery,” *Adv. Funct. Mater.*, vol. 25, no. 33, pp. 5333–5342, 2015.

[13] T. Xu, G. Hwang, N. Andreff, and S. Régnier, “Modeling and swimming property characterizations of scaled-up helical microswimmers,” *IEEE/ASME Trans. Mechatron.*, vol. 19, no. 3, pp. 1069–1079, Jun. 2014.

[14] Y. Hou et al., “Design and control of a surface-dimple-optimized helical microdrill for motions in high-viscosity fluids,” *IEEE/ASME Trans. Mechatron.*, vol. 28, no. 1, pp. 429–439, Feb. 2022.

[15] W. Hu, G. Z. Lum, M. Mastrangeli, and M. Sitti, “Small-scale soft-bodied robot with multimodal locomotion,” *Nature*, vol. 554, no. 7690, pp. 81–85, 2018.

[16] H. Lu et al., “A bioinspired multilegged soft millirobot that functions in both dry and wet conditions,” *Nature Commun.*, vol. 9, no. 1, 2018, Art. no. 3944.

[17] H.-W. Huang, M. S. Sakar, A. J. Petruska, S. Pané, and B. J. Nelson, “Soft micromachines with programmable motility and morphology,” *Nature Commun.*, vol. 7, 2016, Art. no. 12263.

[18] L. Manamanchaiyaporn, T. Xu, and X. Wu, “Magnetic soft robot with the triangular head–tail morphology inspired by lateral undulation,” *IEEE/ASME Trans. Mechatron.*, vol. 25, no. 6, pp. 2688–2699, Dec. 2020.

[19] E. E. Hunter, E. W. Brink, E. B. Steager, and V. Kumar, “Toward soft micro bio robots for cellular and chemical delivery,” *IEEE Robot. Automat. Lett.*, vol. 3, no. 3, pp. 1592–1599, Jul. 2018.

[20] T. Xu, C. Huang, Z. Lai, and X. Wu, “Independent control strategy of multiple magnetic flexible millirobots for position control and path following,” IEEE Trans. Robot., vol. 38, no. 5, pp. 2875–2887, Oct. 2022.

[21] O. Felfoul et al., “Magneto-aerotactic bacteria deliver drug-containing nanoliposomes to tumour hypoxic regions,” *Nature Nanotechnol.*, vol. 11, no. 11, pp. 941–947, 2016.

[22] I. S. Khalil, M. P. Pichel, L. Abelmann, and S. Misra, “Closed-loop control of magnetotactic bacteria,” *Int. J. Robot. Res.*, vol. 32, no. 6, pp. 637–649, 2013.

[23] S. J. Park et al., “New paradigm for tumor theranostic methodology using bacteria-based microrobot,” *Sci. Rep.*, vol. 3, 2013, Art. no. 3394.

[24] L. Ricotti et al., “Biohybrid actuators for robotics: A review of devices actuated by living cells,” *Sci. Robot.*, vol. 2, no. 12, 2017, Art. no. eaaq0495.

[25] M. Medina-Sánchez and O. G. Schmidt, “Medical microbots need better imaging and control,” *Nature*, vol. 545, no. 7655, pp. 406–408, 2017.

[26] M. Rubenstein, A. Cornejo, and R. Nagpal, “Programmable self-assembly in a thousand-robot swarm,” *Science*, vol. 345, no. 6198, pp. 795–799, 2014.

[27] J. Yu, B. Wang, X. Du, Q. Wang, and L. Zhang, “Ultra-extensible ribbon-like magnetic microswarm,” *Nature Commun.*, vol. 9, 2018, Art. no. 3260.

[28] J. Yu, D. Jin, K.-F. Chan, Q. Wang, K. Yuan, and L. Zhang, “Active generation and magnetic actuation of microrobotic swarms in bio-fluids,” *Nature Commun.*, vol. 10, 2019, Art. no. 5631.

[29] L. Yang, J. Yu, S. Yang, B. Wang, B. J. Nelson, and L. Zhang, “A survey on swarm microrobotics,” IEEE Trans. Robot., vol. 38, no. 3, pp. 1531–1551, Jun. 2022.

[30] L. Yang, J. Yu, and L. Zhang, “Statistics-based automated control for a swarm of paramagnetic nanoparticles in 2-D space,” *IEEE Trans. Robot.*, vol. 36, no. 1, pp. 254–270, Feb. 2020.

[31] J. Yu, L. Yang, X. Du, H. Chen, T. Xu, and L. Zhang, “Adaptive pattern and motion control of magnetic microrobotic swarms,” IEEE Trans. Robot., vol. 38, no. 3, pp. 1552–1570, Jun. 2021.

[32] Q. Wang et al., “Ultrasound Doppler-guided real-time navigation of a magnetic microswarm for active endovascular delivery,” *Sci. Adv.*, vol. 7, no. 9, 2021, Art. no. eabe5914.

[33] T. Xu, Y. Guan, J. Liu, and X. Wu, “Image-based visual servoing of helical microswimmers for planar path following,” *IEEE Trans. Automat. Sci. Eng.*, vol. 17, no. 1, pp. 325–333, Jan. 2020.

[34] L. Yang, Y. Zhang, Q. Wang, and L. Zhang, “An automated microrobotic platform for rapid detection of C. diff toxins,” IEEE Trans. Biomed. Eng., vol. 67, no. 5, pp. 1517–1527, May 2020.

[35] M. Salehizadeh and E. D. Diller, “Path planning and tracking for an underactuated two-microrobot system,” *IEEE Robot. Automat. Lett.*, vol. 6, no. 2, pp. 2674–2681, Apr. 2021.

[36] T. Li et al., “Autonomous collision-free navigation of microvehicles in complex and dynamically changing environments,” *ACS Nano*, vol. 11, no. 9, pp. 9268–9275, 2017.

[37] Z. Yang, L. Yang, and L. Zhang, “Autonomous navigation of magnetic microrobots in a large workspace using mobile-coil system,” *IEEE/ASME Trans. Mechatron.*, vol. 26, no. 6, pp. 3163–3174, Dec. 2021.

[38] S. Campbell, N. O’Mahony, A. Carvalho, L. Krpalkova, D. Riordan, and J. Walsh, “Path planning techniques for mobile robots a review,” in *Proc. IEEE 6th Int. Conf. Mechatron. Robot. Eng.*, 2020, pp. 12–16.

[39] S. S. Ge and Y. J. Cui, “Dynamic motion planning for mobile robots using potential field method,” *Auton. Robots*, vol. 13, no. 3, pp. 207–222, 2002.

[40] W.-G. Han, S.-M. Baek, and T.-Y. Kuc, “Genetic algorithm based path planning and dynamic obstacle avoidance of mobile robots,” in *Proc. IEEE Int. Conf. Syst., Man, Cybern.. Comput. Cybern. Simul.*, vol. 3, 1997, pp. 2747–2751.

[41] M. Al-Khatib and J. J. Saade, “An efficient data-driven fuzzy approach to the motion planning problem of a mobile robot,” *Fuzzy Sets Syst.*, vol. 134, no. 1, pp. 65–82, 2003.

[42] J. Yu, L. Yang, and L. Zhang, “Pattern generation and motion control of a vortex-like paramagnetic nanoparticle swarm,” *Int. J. Robot. Res.*, vol. 37, no. 8, pp. 912–930, 2018.

[43] L. Zheng et al., “3D navigation control of untethered magnetic microrobot in centimeter-scale workspace based on field-of-view tracking scheme,” *IEEE Trans. Robot.*, vol. 38, no. 3, pp. 1583–1598, Jun. 2021.

[44] T. Ju, S. Liu, J. Yang, and D. Sun, “Rapidly exploring random tree algorithm-based path planning for robot-aided optical manipulation of biological cells,” *IEEE Trans. Automat. Sci. Eng.*, vol. 11, no. 3, pp. 649–657, Jul. 2014.

[45] H. Chen and D. Sun, “Moving groups of microparticles into array with a robot–tweezers manipulation system,” IEEE Trans. Robot., vol. 28, no. 5, pp. 1069–1080, Oct. 2012.

[46] L. Janson, E. Schmerling, A. Clark, and M. Pavone, “Fast marching tree: A fast marching sampling-based method for optimal motion planning in many dimensions,” *Int. J. Robot. Res.*, vol. 34, no. 7, pp. 883–921, 2015.

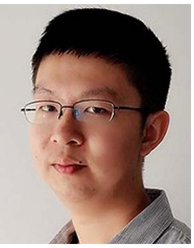

Yuezhen Liu (Student Member, IEEE) received the B. Eng. degree in automation from the Harbin Institute of Technology, Shenzhen, China, in 2021. He is currently working toward the Ph.D. degree in computer and information engineering with the School of Science and Engineering, The Chinese University of Hong Kong, Shenzhen, China.

His research interests include vision based intelligent control and biomedical applications of microrobots.

Hui Chen (Student Member, IEEE) received the B.Eng. and M.S. degrees in ocean engineering from Harbin Engineering University, Harbin, China, in 2018 and 2021. He is currently working toward the Ph.D degree in computer and information engineering with the School of Science and Engineering The Chinese University of Hong Kong, Shenzhen, China.

His research interests include intelligent control and biomedical applications of micronanorobotic swarms.

Qian Zou (Student Member, IEEE) received the B.Eng. degree in mechanical engineering from Hainan University, Haikou, China, and a joint M.Sc. degree in sensor and imaging system from the University of Glasgow, Glasgow, U.K. and University of Edinburgh, Edinburgh, U.K. He is currently working toward the Ph.D. degree in computer and information engineering with the School of Science and Engineering the Chinese University of Hong Kong, Shenzhen, China.

His research interests include path planning and tracking control of magnetic microrobots.

Xingzhou Du (Member, IEEE) received the B.Eng. degree in automation science and technology from Xi'an Jiaotong University, Xi'an, China, in 2017, and the Ph.D. degree in biomedical engineering from the Chinese University of Hong Kong, Hong Kong, in 2021.

He is currently a Research Associate Scientist with the Shenzhen Institute of Artificial Intelligence and Robotics for Society, Shenzhen, China. His research interests include the development of electromagnetic systems and the control methods for magnetic microrobots.

Dr. Du was the recipient of the Toshio Fukuda Best Paper Award in Mechatronics at 2020 IEEE International Conference on Advanced Robotics and Mechatronics.

Yibin Wang (Student Member, IEEE) received the B.Eng. degree in materials processing from the Harbin Institute of Technology, Weihai, China, in 2018, and the M.Sc. degree in materials science from Carnegie Mellon University, Pittsburgh, PA, USA, in 2019. He is currently working toward the Ph.D. degree in materials science and engineering with the School of Science and Engineering, The Chinese University of Hong Kong, Shenzhen, China.

His research interests include magnetically controlled soft robotics.

Jiangfan Yu (Member, IEEE) received the B.Eng. degree in automation from the Harbin Institute of Technology, Harbin, China, in 2014, and the Ph.D. degree in mechanical and automation engineering from the Chinese University of Hong Kong, Hong Kong, in 2018.

He is currently an assistant professor with the School of Science and Engineering and an Adjunct Assistant Professor with the School of Medicine, the Chinese University of Hong Kong, Shenzhen. He is the Deputy Director and the Institute-level PI in Micro-Nanorobotics Center of Shenzhen Institute of Artificial Intelligence and Robotics for Society. He worked as a Postdoctoral Fellow with Chinese University of Hong Kong, from 2018 to 2019, and with the University of Toronto, Toronto, ON, Canada, from 2019 to 2020. His research interests include small-scaled robotics, control and medical robotics.

Dr. Yu was the recipient of the IEEE/ASME Transactions on Mechatronics Best Paper Finalist in 2020, Nature Communications Top 50 Physics Articles in 2018, and Hong Kong Young Scientist Shortlist in 2018. He is an Associate Editor for IEEE ROBOTICS AND AUTOMATION LETTERS, and a Guest Editor for Micromachines, Frontiers in Robotics and AI, and *Journal of Healthcare Engineering*.